December 2021

A High-Bandwidth, Spectrally Broad Photodetector Based on Optically-Induced Seebeck Effect

Niloufar Yavarishad
University of Wisconsin-Milwaukee

A HIGH-BANDWIDTH, SPECTRALLY BROAD PHOTODETECTOR BASED ON OPTICALLY- INDUCED SEEBECK EFFECT

by

Niloufar Yavarishad

A Thesis Submitted in

Partial Fulfillment of the

Requirements for the Degree of

Master of Science

in Engineering

at

The University of Wisconsin-Milwaukee

December 2021

ABSTRACT

A HIGH-BANDWIDTH, SPECTRALLY BROAD PHOTODETECTOR BASED ON OPTICALLY- INDUCED SEEBECK EFFECT

by

Niloufar Yavarishad

The University of Wisconsin-Milwaukee, 2021
Under the Supervision of Professor Prasenjit Guptasarma

In this thesis, we engineered a fast response high bandwidth self-powered infrared photodetector based on optically induced Seebeck effect in Cd_3As_2 operating at room temperature. The metal-semimetal-metal device was subject to transient photo-response tests using high-frequency lock-in modulation techniques. Our photodetector demonstrates a Seebeck voltage under the off-center illumination of a laser with the wavelength of 1064 nm, due to a temperature gradient. The photocurrent is readily registered at a modulation frequency of 6 kHz and further analysis indicates the sensor intrinsic bandwidth is predicted to approach the terahertz range. The responsivity of the sensor is 0.27 mA/W at room temperature and the photocurrent is found to be dependent on the modulation frequency and the optical power. Our study reveals that Cd_3As_2 is a promising candidate for a fast response, high bandwidth spectrally broad device applications in optoelectronics.

To

My Beloved Parents,

My Grandmother,

and My One and Only Brother

TABLE OF CONTENTS

LIST OF FIGURES

PAGE

ACKNOWLEDGEMENTS

From the bottom of my heart, I would like to thank my advisor Prof. Prasenjit Guptasarma who inspires me with his exemplary intellect and demeanor. I greatly appreciate his continued support, encouragement, kindness, and enthusiasm for high quality research.

I would like to express my deepest gratitude to my committee members, Prof. George Hanson, and Prof. Habib Tabatabai for their valuable insights and constructive feedbacks and supports. I would also like to extend my appreciation to Dr. Steven Hardcastle and Dr. Heather Owen for their experimental advice at the Advanced Analysis Facility and the Electron Microscope Laboratory.

I would like to acknowledge the support of Prof. Nikolai Kouklin at the UWM Nanotechnology Research Laboratory to make this work happen, and our collaborator Prof. Chris Weber at the Santa Clara University. I would also like to thank my lab-mates Tahereh Hosseini, Elaheh Kheirandish, Jacob Alward, Casey Marnocha, Yanan Li, Heather Pace, William Rexhausen, and Christian Parsons for their collaboration in research and thesis preparation.

My deepest and most heartfelt gratitude is to my beloved parents, Mahboubeh and Ebrahim, my grandmother, Fatemeh, and my one and only brother, Masoud who have sacrificed a lot for me to be in the graduate school in a foreign country. And my sincere appreciation goes to my uncles, Peyman and Mehrdad, and my aunts, Leila and Sareh for their continuous supports. I would also like to thank my dearest friends, Zamzam, Masha, Roya, Shima and Mohsen, and the senior admin specialist at our college, Mrs. Elisabeth Warras without whom this journey would not have been possible.

At last, but not least, I would like to thank me for believing in me, doing the hard work and for never quitting.

THIS PAGE INTENTIONALLY LEFT BLANK.

Chapter 1.

Overview

Infrared spectroscopy and detection have been widely used since 1880 when William Herschel discovered the infrared portion of the electromagnetic spectrum (Figure 1-1) which is not visible to the naked eye [1]. Since the earliest development of the IR detectors by Macedonio Melloni in the mid-19th century [3], there has been significant progress in our understanding of the mechanisms, and in techniques and material development for IR detection. IR detectors are being utilized in military for navigation, night vision and weapon detection, as well as other applications in academic research, communications, aerospace, and medical imaging. We can detect and study structures and processes in the Infrared range (0.7μm- 1mm) of spectrum that are effectively invisible in the optical range (0.4-0.7 μm) or cannot be detected in the absence of the visible light (night vision)[4].

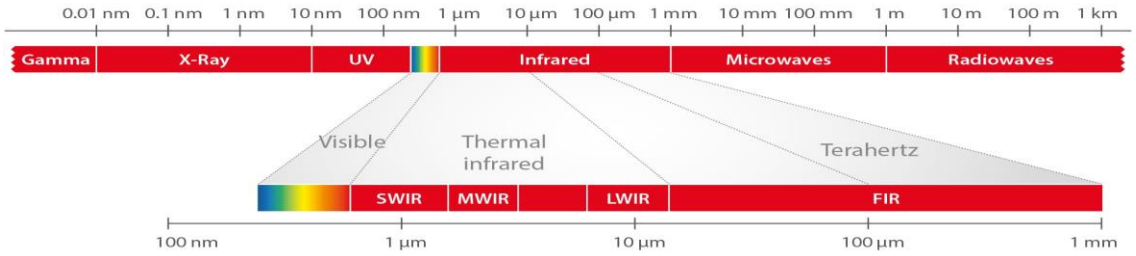

Figure 1-1. Electromagnetic Spectrum [2].

For example, in Figure 1-2, in the visible-light image (left) due to the dense gas clouds, most of the stars cannot be detected. However, when using an IR detector, they are detectable through the gas or dust.

Figure 1-2. Image of Carina Nebula in the visible range (left) and the Infrared range (right) obtained by the Hubble telescope [5].

In Figure 1-3, comparing the right and left images, it is shown that our eyes cannot see the infrared waves emitted from human body or animals but with the use of IR detectors in thermal imaging we can detect them.

Figure 1-3. Thermal imaging of a dog obtained by NASA/JPL-Caltech; temperatures are shown in degrees Fahrenheit [5].

There are two main classes of the IR photodetectors: quantum or photon detectors and thermal detectors. In the following section these categories will be discussed with a focus on the thermal detectors.

1.1 Introduction to Infrared Photodetectors

As was mentioned above, IR detectors can be roughly divided into two classes: thermal detectors and photon detectors. Photon detectors work based on photovoltaic (PV) and photoconductive effects and are well-suited for applications ranging from short-wavelength to near-infrared range. There has been a significant improvement in terms of their performance, speed, and responsivity over the years [4]. However, as the photoresponse is dependent on the electron-hole generation, and the built-in or applied external bias in a photon detector, the properties of the photon detector are limited by the bandgap of the photodetector material [6]. Also, due to the importance of the applications of the long wavelength infrared, most of the photon detectors are not good candidates. Additionally, only photon detectors based on the narrow-bandgap semiconductors (such as HgCdTe) and quantum wells (such as GaAs / InGaAs) can be used for higher wavelength detection [7, 8]. Other problems with photodetectors is that they exhibit a large dark current at room temperature and require cooling. With the burden of the cryogenic cooling added to the photodetector, the device becomes more complicated, expensive, and heavier to carry. This is not suitable for applications in, e.g., aerospace.

In contrast to photon detectors, thermal detectors have spectrally broad bandwidth up to terahertz. Some of them operate at room temperature [9]. In a thermal detector, the absorption of the incoming radiation changes the temperature of the device material and this temperature gradient then alters a specific quantity of the detector. Well-known thermal detectors in which the electrical properties change with temperature are bolometers, thermocouple/thermopile, and pyroelectric detectors. We will discuss these in further details in the following section.

1.2 Thermal Photodetectors

As mentioned earlier, thermal detectors work based on the measurements of temperature-dependent properties. For instance, in a bolometer, the temperature gradient caused by an IR radiation changes the conductance of the device material. In a pyroelectric detector, the spontaneous polarization varies with the temperature difference. In a thermocouple, voltage is generated at the junction of the different metals (a thermopile is several thermocouples connected in series or parallel). The voltage generated in a thermocouple is known as the Seebeck voltage. There is another type of thermal detector which is known as photo-thermo-voltaic detector (PTV). PTVs also perform based on the Seebeck voltage. The infrared photodetector designed and described in this study utilizes the Seebeck effect.

1.3 Seebeck Effect

In 1821, the Seebeck effect was discovered by Thomas Seebeck. It refers to an electromotive force formed by a temperature differential in metals or semiconductors [10]. When a temperature difference is created along a conductive material, the free charge carriers, such as electrons in metals and n-type semiconductors (or holes in a p-type semiconductors) cause a net diffusion of charge carriers from the warmer side of the material to the cooler side. As the charges diffuse away, there are more mobile carriers at the cold side than the hot side, leading to an electric field. As a result of the temperature gradient, eventually at equilibrium an electrochemical potential will form which is known as the Seebeck voltage. Figure 1-4 demonstrates the Seebeck effect in a n-type and p-type semiconductor.

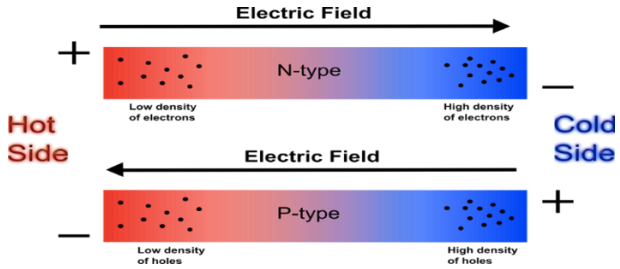

Figure 1-4. Seebeck effect: Electrochemical potential generation due to temperature gradient in n-type semiconductor (up) and p-type semiconductor (down) [11].

1.4 Thesis Outline

In this work, we used Cd_3As_2 platelets, which were grown by a low-temperature chemical vapor deposition technique, to build a spectrally broad bandwidth PVT sensor that operates at room temperature. In Chapter 2, the growth mechanism of Cd_3As_2 platelets as well as the methods of elemental and optical materials characterization along with the results are discussed in detail.

Chapter 3 describes the device preparation and the dependency of current- voltage on temperature. The temperature dependent thermopower measurements are also provided.

Lastly, the PTV device performance is assessed in Chapter 4. A short summary and potential future study of the thesis subject matter are presented in Chapter 5.

Chapter 2.

Synthesis and Characterization Methods of Crystalline Cd_3As_2 platelets

2.1 Background

Cadmium Arsenide (Cd_3As_2) is a three-dimensional Dirac semimetal [12-14] that exhibits large electron mobility of 10^7 cm^2 V^{-1} s^{-1} at 5 kelvin [15], strong IR-light absorption, low thermal conductivity and large thermopower of 600 µV/ K in the temperature range of 300-400 K [16]. Therefore, it is well suited for applications ranging from ultra-fast IR sensors to energy conversion. In this work, Cd_3As_2 platelets were fabricated by the low- temperature Chemical Vapor Deposition (CVD) technique. The platelets were investigated by visual optical microscopes and scanning electron microscopes (SEM) followed by analysis via energy dispersive spectroscopy (EDS) and Fourier Transform Infrared spectroscopy (FTIR). The synthesis and characterization of Cd_3As_2 platelets, CVD technique, SEM, EDS and FTIR methods are discussed in the following sections.

2.1.1 Chemical Vapor Deposition Technique

Chemical Vapor deposition (CVD) is a widely used materials growth technique to produce high quality thin films. In general, it involves the formation of a thin solid film on a substrate material via chemical reaction of vapor-phase precursors. It can thus be distinguished from physical vapor deposition (PVD) processes, such as evaporation and reactive sputtering, which involve the adsorption of atomic or molecular species on the substrate. The chemical reactions of precursor species occur both in the gas phase and on the substrate. Reactions can be promoted or initiated by heat (thermal CVD), higher frequency radiation such as UV (photo-assisted CVD), or a plasma (plasma-enhanced CVD) [17, 18].

A more detailed picture of the basic physicochemical steps in an overall CVD reaction is illustrated

in Figure 2-1, which indicates several key steps:

1- The precursors evaporate or sublimate in the furnace and, with the help of the carrier gas, flow into the chamber.

2- The reactions in the gas phase produce reactive intermediates and gaseous by-products.

3- Reactants are then transported to the substrate surface and are absorbed by the substrate.

4- Surface diffusion, nucleation and surface chemical reactions lead to film formation.

5- The byproducts are exhausted out of the reactor along with the carrier gas.

Figure 2-1 illustrates the mechanisms that occur during the CVD technique.

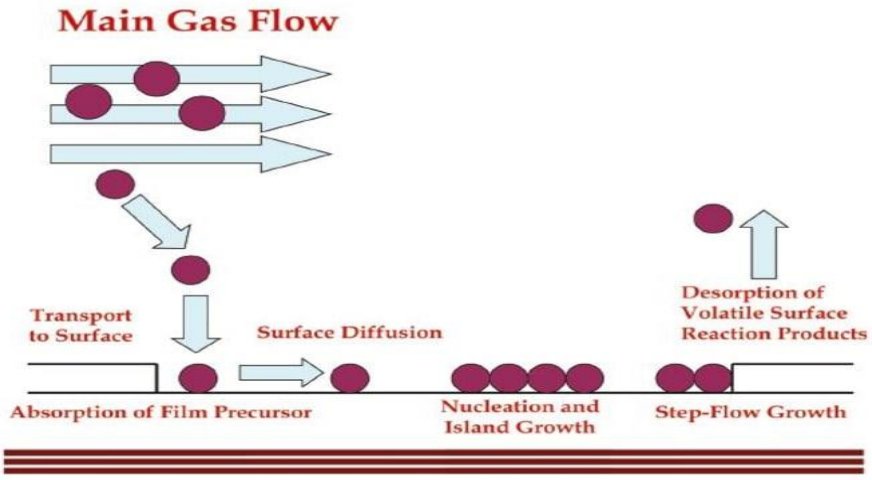

Figure 2-1. Schematic diagram of the mechanisms that occur during the CVD process [19].

Variant structures of materials require different CVD configurations such as hot-wall furnaces and cold-wall reactors, and growth conditions at high vacuum to atmospheric pressures, with or without using the carrier gases in the temperature ranging from 200 to 1600 °C. In this work, we used a horizontal hot-wall furnace for low-temperature CVD, discussed later.

2.1.2 Scanning Electron Microscopy

Scanning electron microscopy (SEM) is the most widely used electron microscopy technique to produce detailed, magnified, and high-resolution images of an object by scanning its surface. As is shown in Figure 2-2, a stream of primary electrons generated by an electron gun is focused onto the sample surface using an anode and a series of magnetic lenses in a vacuum chamber (the stage also has positive charge). The incident high energy electrons strike the specimen and are scattered by the atoms of the specimen, resulting in secondary electrons and back-scattered electrons collected by the electron detector. These provide the signal for forming images in SEM.

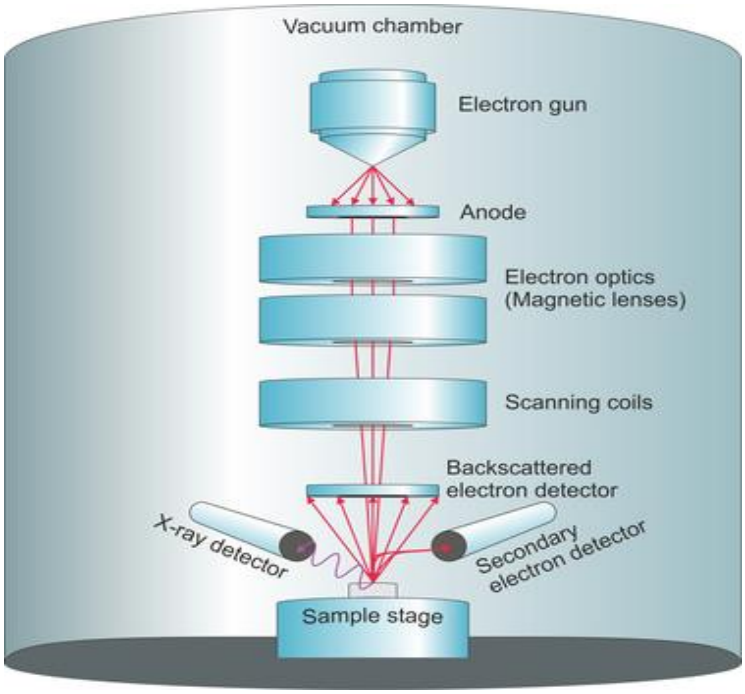

Figure 2-2. Schematic of a scanning electron microscope equipped with X-ray energy dispersive spectrometer [20].

In the interaction zone, as illustrated in Figure 2-3, secondary electrons escape from a volume near the specimen surface within the depth of 5-50 nm. The backscattered electrons with the

energy close to the high-energy incident electrons escape from a deeper depth of 50-300 nm under the specimen surface [21].

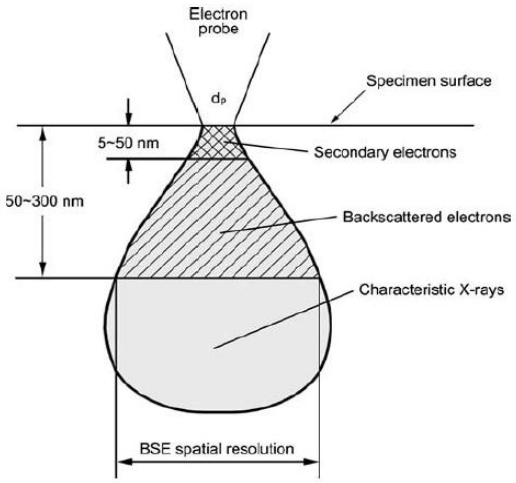

Figure 2-3. The interaction area of electrons and sample atoms below the sample surface [21].

2.1.3 Energy Dispersive X-ray Spectroscopy

In addition to the secondary and backscattered electrons scattered from the sample, characteristic X-rays are also generated in the interaction zone, Figure 2-3. When accelerated electrons kick out an electron from the electron shell around an atomic nucleus, an electron from a higher energy shell takes its place and releases the difference in energy in the form of X-rays. The energy released, in the X-ray regime, is dependent on the energy difference of the shells and is characteristic of the specific element from which the X-ray emanates. In Energy Dispersive X-ray Spectroscopy (EDS or EDX), these characteristic X-rays are detected and identified in order to examine the chemical elements of a material. EDS detector is often included as a part of SEM (Figure 2-2) equipment. The probed depth in EDX analysis is below 300nm and the typical resolution of energy dispersion is about 150-200 eV [22].

2.1.4 Fourier Transform Infrared Spectroscopy

One of the most used vibrational spectroscopies in materials science is the Fourier transform infrared spectroscopy (FTIR). The infrared spectrum is obtained using Fourier transform method in a whole range of wavenumbers simultaneously in FTIR. The key component in the FTIR system is the Michelson interferometer, illustrated in Figure 2-4.

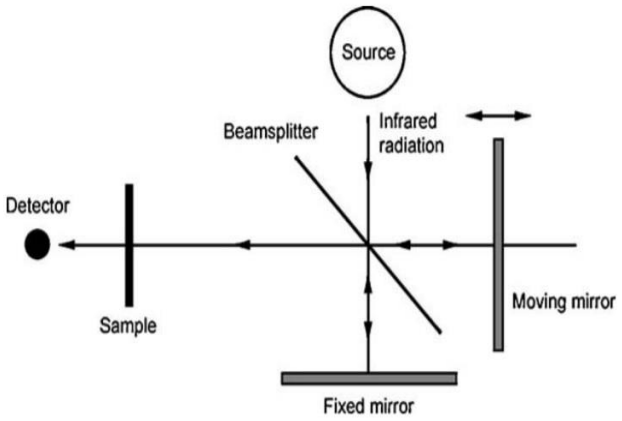

Figure 2-4. Optical diagram of a Michelson interferometer in FTIR [23].

The IR enters the interferometer and then the beam splitter transmits half of the IR radiation to the fixed mirror and reflects the other half to the moving mirror. After reflecting from the mirrors, the two split beams combine at the beam splitter again before irradiating the sample. It should be mentioned that the function of the moving mirror is to change the optical path length to generate the light interference. A plot of light interference intensity as function of optical path difference is called an interferogram, Figure 2-5.

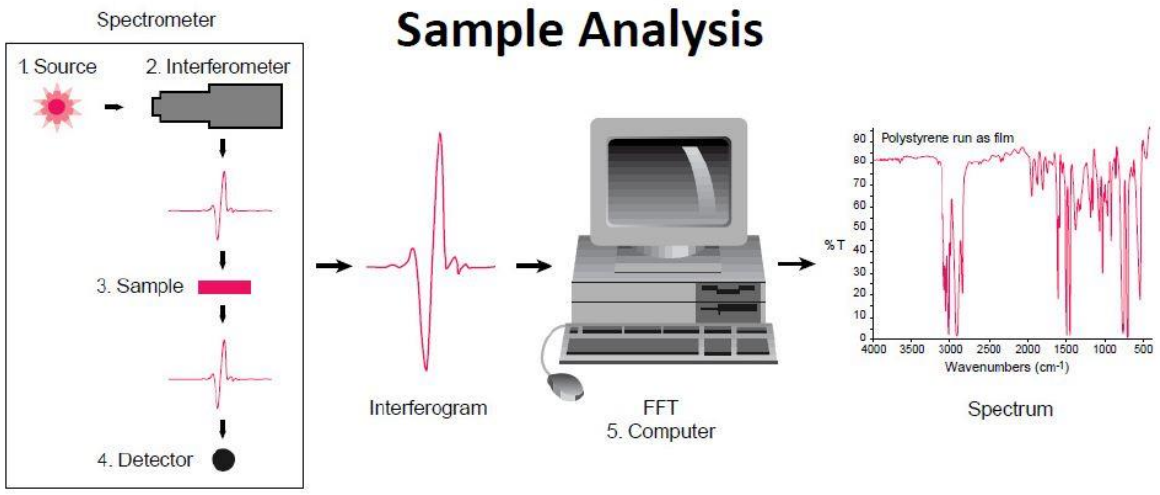

Figure 2-5. Fourier transform infrared spectroscopy [23].

An interferogram irradiating the sample is the sum of sinusoidal waves with a range of wavelengths. The detector receives interferogram signals which are transmitted to a sample (or reflected from a sample). An FTIR instrument uses the Fourier transform to convert the intensity versus optical path difference obtained from the interferogram to the intensity versus wavenumber. Therefore, using the light intensity versus wavenumber plot (spectrum), we can investigate the transmission or absorption bands for a certain material [23].

2.2 Results and Discussion

Cd_3As_2 platelets were grown in a horizontally oriented hot-wall chemical vapor deposition furnace in atmospheric pressure. Pure (99.99%) polycrystalline Cd_3As_2 powder from Sigma-Aldrich was used as a precursor and a ceramic boat was utilized as growth substrate. Prior to the growth, to prevent oxidation, we minimized the partial pressure of O_2 by flushing the furnace several times. We reduced its base pressure to ~ 1mTorr and then refilled it with 99.99% pure Argon gas as the

carrier gas inside the furnace. Using an IR temperature sensor, we monitored the furnace temperature which was gradually increased from room temperature (25°C) to 700°C as measured at the geometric center of the quartz tube of the furnace. Precursor vapors of Cadmium and Arsenic were transported at the flow rate of ~ 0.2 SCCM with the help of flowing Argon gas. The temperature of the middle of the furnace was kept at 700 °C for approximately an hour and then the reactor was cooled down to the room temperature at the rate of 5 °C min^{-1}. We observed up to centimeter-long shiny crystallites of Cd_3As_2 nucleated on the surface of the ceramic boat placed in the temperature range of 200° C to 130° C [16]. The schematic of the CVD growth of Cd_3As_2 platelets and the temperature profile is shown in Figure 2-6.

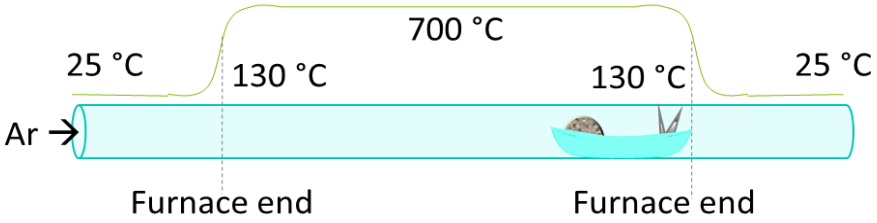

Figure 2-6. Schematic of the CVD furnace and temperature profile [16].

We maintained the growth temperature at or below 225 ^{0}C to avoid phase transitions accompanied by defect formation. As is shown in the phase diagram of Cadmium Arsenide, Figure 2-7, upon cooling, Cd_3As_2 undergoes multiple polymorphic solid-solid transitions at 595, 465 and 225 ^{0}C, respectively.

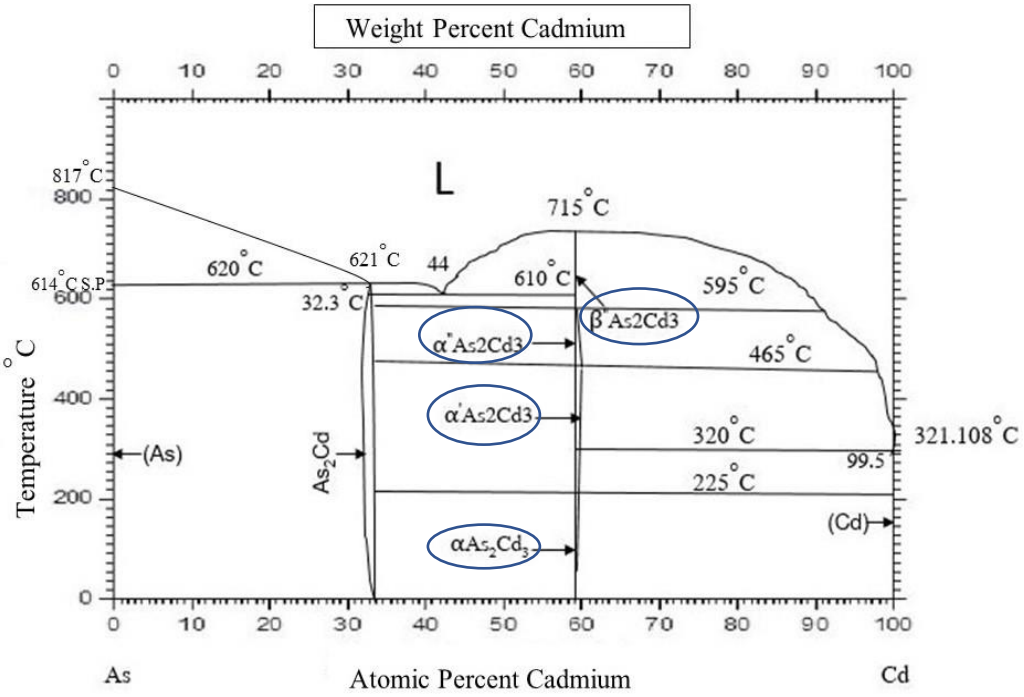

Figure 2-7. Phase diagram of Cd_3As_2 [24].

Energy dispersive X-ray spectra was performed using a Hitachi S4800 ultra-high resolution field emission scanning electron microscope to confirm the stoichiometry of the Cd_3As_2. The resultant spectrum is shown in Figure 2-8. Cd_3As_2 platelets had elongated, planar flat top surface typical of single crystals with the thickness of 10 µm. We confirmed that we have pure Cd_3As_2 with the atomic ratio of Cd to As 65 to 35, which slightly deviates from the ideal 60-40 Cd to As atomic ratio of the polycrystalline Cd_3As_2 precursor, implying that Cd_3As_2 platelets were slightly Cd-enriched and n-doped type platelets.

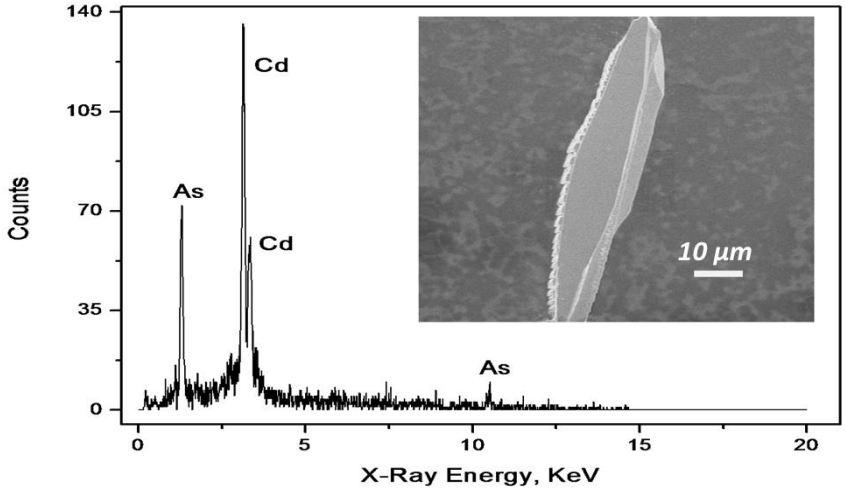

Figure 2-8. Energy dispersive x-ray of a Cd_3As_2 platelet. The inset shows a top-view SEM image of the sample.

Next, the optical absorption of the sample was collected in the spectral range of 0.1 to 0.5 eV at room temperature. The measurement was done using a Bruker, Tensor-27 Fourier transform infrared spectrometer with a Hyperion optical microscope (15x objective) [25]. The platelet was placed on a Au coated substrate to limit substrate contribution (it was also used for background subtraction). The spectrometer resolution was 1 cm^{-1} and the infrared laser wavelength was 1064 nm. The FTIR absorption spectrum is shown in Figure 2-9. Above 0.35 eV, the absorption was primarily interband and is around 16%. But as energy goes down the free carrier absorption goes up, reaching around 30% with an absorption coefficient of 350 cm^{-1} at 0.1 eV. This result suggests the photodetector based on Cd_3As_2 will remain highly sensitive to free carrier absorption at long wavelengths.

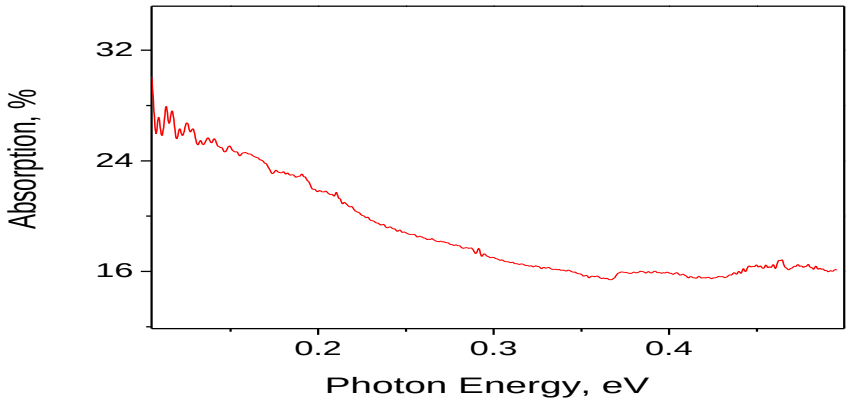

Figure 2-9. Fourier transform infrared spectrum of Cd_3As_2 platelet.

Chapter 3.

Device Preparation and Transport Studies

3.1 Metal-Semimetal-Metal PTV Device

We fabricated a photo-thermo-voltaic (PTV) sensor by placing a platelet with the width of 4μm and thickness of 10μm across a gap of 3 mm formed by two Copper electrodes (Cu) using micro-manipulators. Glass was used as a substrate and Cd_3As_2 was connected to Cu by melting Indium (In) at the contacts as illustrated in Figure 3-1.

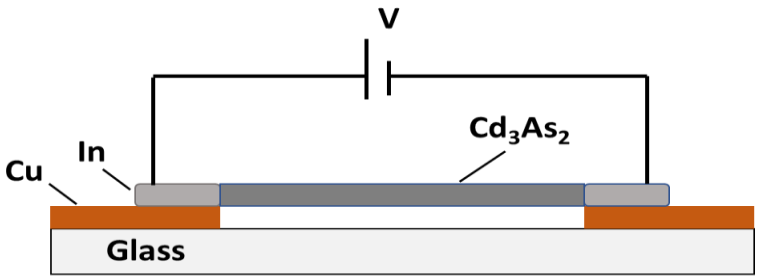

Figure 3-1. Schematic of a PTV device based on Cd_3As_2 platelet.

3.2 Temperature dependent Current-Voltage Measurements

To investigate the temperature dependence of the electrical conductivity, σ, we conducted charge-transport characteristics. The device was placed in a heating-cooling stage (Instec HCS302) and the currents versus voltages (I-Vs) were measured with a Keithley 236 Source-Measure Unit (SMU) in the temperature range of 220 to 620 k with a bias range of ±5 mV. As is shown in Figure 3-2, the I-Vs are ohmic, with the conductivity exhibiting a monotonic decrease with temperature [16].

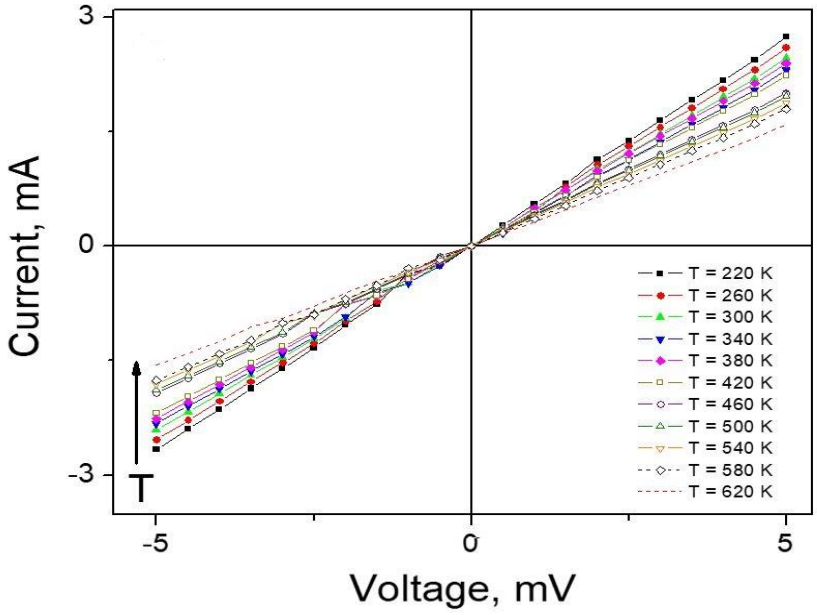

Figure 3-2. T-dependent I-Vs in the temperature range of 220 to 620 k [16].

Having the temperature dependent I-Vs, we then calculated and investigated the dependence of differential conductance, S, on temperature. As shown in Figure 3-3, the conductance decreases linearly (0.55 to 0.3) with increasing the temperature, which is typical of semimetals. This implies that the contribution of the electrodes (contacts) and the bolometric effects to the photo response is negligible.

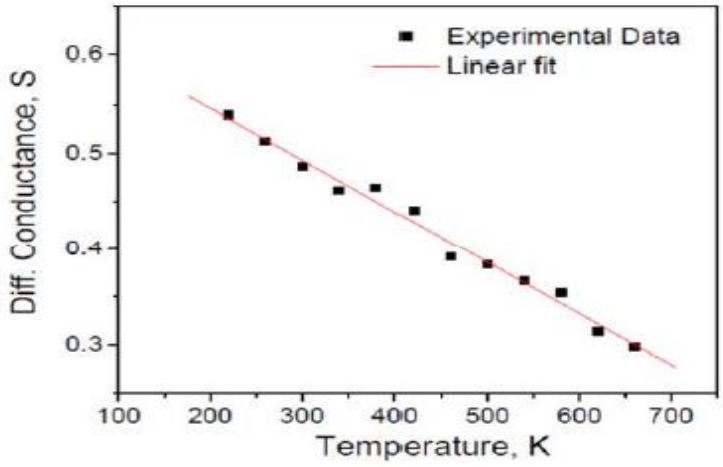

Figure 3-3. Differential conductance vs temperature [26].

3.3 Temperature dependent Thermopower Characteristics

Seebeck coefficient, also known as thermopower, is defined as the magnitude of a thermoelectric voltage in response to a temperature gradient across the material. Therefore, in order to measure the Seebeck coefficient, the Seebeck voltage induced per unit temperature gradient in the sample must be measured. To measure the Seebeck voltage, the device was placed in a Janis closed-cycle cryostat, the pressure was pumped down to approximately 10^{-4} Torr, and the measurement was done in the temperature range of 220 to 620 K. We, then illuminated one of the metal contacts of the device by a CW-1064 nm solid-state laser though an optical access window of the cryostat to create a temperature difference of ~ 5k as measured by a thermocouple. The I-V (current-voltage) data at each temperature were collected using Keithley 236 SMU. The thermally induced Seebeck voltages were identified as the open-circuit voltage (V_{OC}) of the I-Vs. The I-V plots and other details of this measurement are further discussed in Ref 16.

The thermopower versus temperature was then extracted using the V_{OC} s at each temperature. The resultant plot is shown in Figure 3-4.

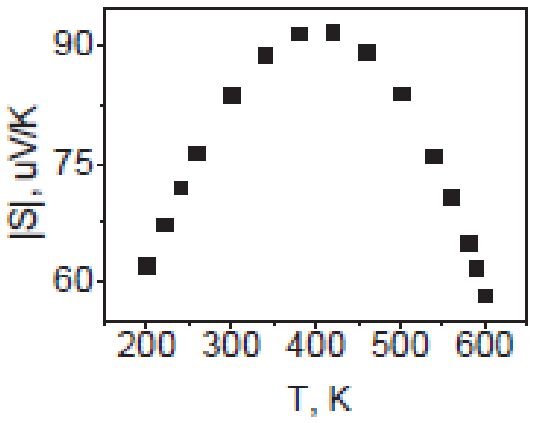

Figure 3-4. Thermopower vs temperature of a Cd_3As_2 platelet [26].

The thermopower was positive, meaning that the Seebeck coefficient, S, was negative and that the maximum value of the thermopower appeared to be at 385 K. This is attributed to the ambipolar heat transport. As $S < 0$, the majority carriers were confirmed to be electrons, n-type doped, at a low temperature [16].

Chapter 4.

Photo-thermo-voltaic Device Characteristics

To test the operation of our device, we measured the current versus voltage at room temperature in the applied bias range of -0.5 V to 0.5 V without illumination of IR laser (dark current measurement). As shown in Figure 4-1, the I-V is non-rectifying/ Ohmic and the Open Circuit voltage is zero (at I=0, V_{OC}=0).

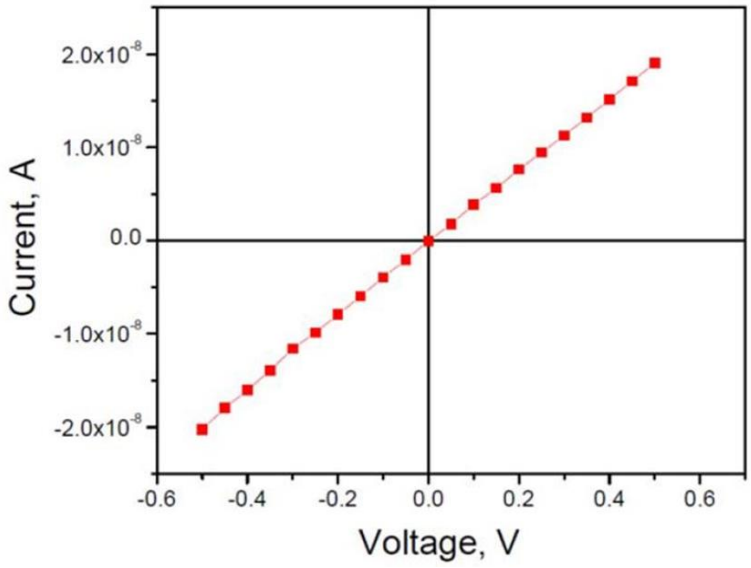

Figure 4-1. Dark I-V at room temperature in the range of ± 0.5V of Cd_3As_2.

4.1 Position dependent Measurements

We observed that under the illumination of the CW-1064 nm solid-state laser, Figure 4-2, the I-Vs remain Ohmic but are shifted vertically except for one point, the center of the device, Figure 4-3. Therefore, we concluded that under the off-center illumination, there is an open-circuit

voltage ($V_{OC}=\Delta V_{emf}$) on the order of 0.1 mV, indicating that the device could operate as a thermovoltaic cell. The net direct current generated by the device is given as

$$I_{dc} = \frac{V_{bias} + \Delta V_{emf}}{R_{sensor} + R_c}$$

V_{bias}, R_{sensor}, and R_c are applied bias, resistance of Cd_3As_2 and the contact electrical resistance, respectively, with R_c being negligible compared to R_{sensor} ($R_{sensor} \gg R_c$).

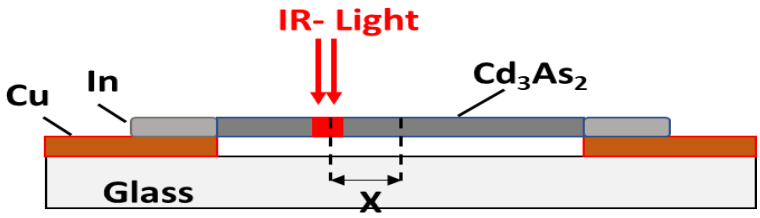

Figure4-2. Schematic of the Cd_3As_2 PTV device under the off-center illumination by an IR laser of 1064 nm wavelength.

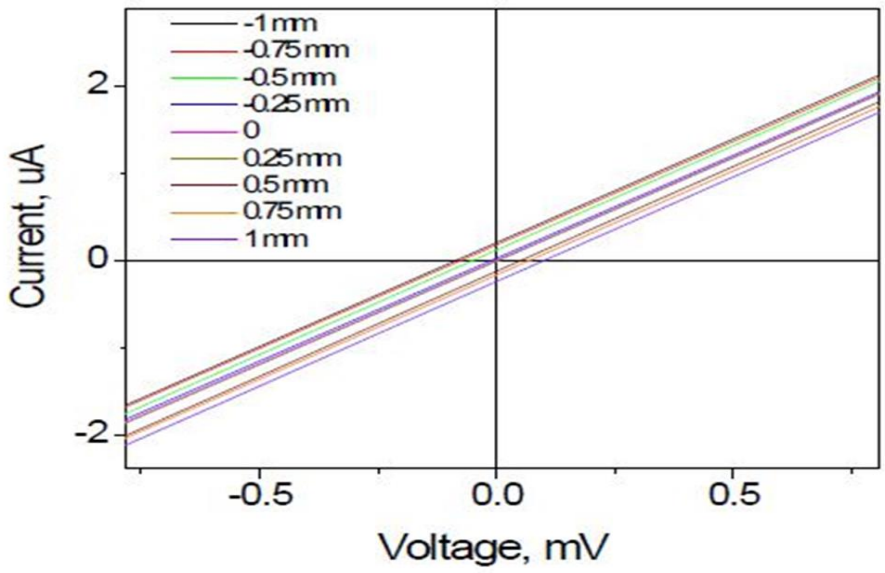

Figure 4-3. I-V characteristics obtained at different laser position.

Figure 4-4 shows the current versus ΔV_{emf} obtained for different laser beam position, X, measured from the center of the device. Figure X schematically shows the IR beam position at the center of the device with length L in which T_h and T_c are high and low temperature, respectively.

$$\Delta V = S\left[T(0) - T\left(\frac{-L}{2}\right)\right] + S\left[T\left(\frac{L}{2}\right) - T(0)\right] = S(T_h - T_c + T_c - T_h) = 0$$

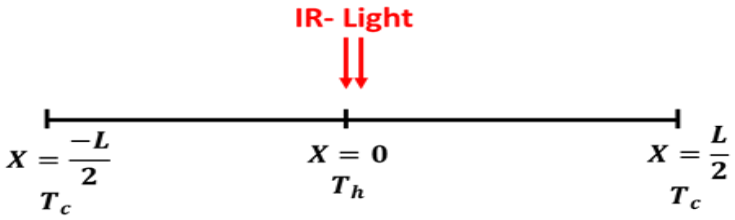

Figure 4-4. Laser beam position at the center of the device.

Short-circuit photocurrent values (I_{SC} at V=0) were obtained using the I-Vs for different positions of the laser beam, measured from center of the device. The result is plotted in Figure 4-5.

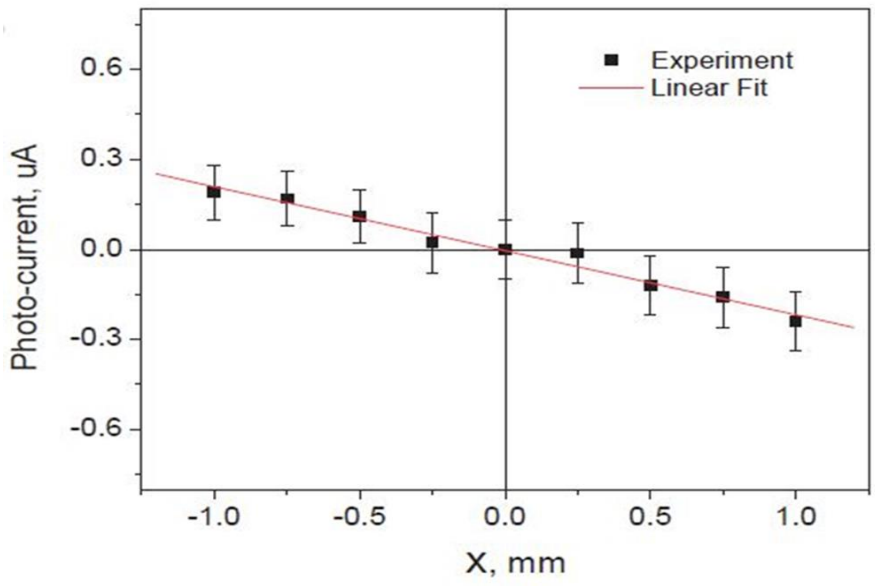

Figure 4-5. Position dependent photocurrent at zero bias, the red line is a linear fit of the data.

As shown in Figure 4-5, the short-circuit photocurrent changes linearly with respect to X, and reverses its sign at the middle of the device (X=0). We found that the right and left temperature difference is equal when the center of the device is illuminated by IR laser, indicating that the two photo-induced voltages cancel each other, resulting in zero net current.

Recalling the thermopower, S, dependency on temperature, as discussed in Chapter 3, we observed that the maximum photocurrent occurred at 385 K, which is the peak thermopower.

The responsivity of the PTV device, the ratio of the photocurrent to the optical power at room temperature, was calculated to be 0.27 mA/W.

4.2 Discussion of the origin of the photocurrent

Photocurrent can be generated due to the bolometric effect, electron-hole generation, Schottky junctions and the photo-induced Seebeck effect. We observed that the bolometric effect was negligible for our sensor. As discussed earlier in Chapter 3, the conductance of the metal-C_3As_2-metal device was slightly dependent on the temperature. This dependence of the conductance on the temperature, although insignificant, excludes "electron-hole generation" as a cause of the photocurrent. Otherwise, the photocurrent would not disappear at the center of the device (X=0) and the conductivity would be increased. As is obvious from the Ohmic/ non-rectifying I-Vs for the sensor, formation of a Schottky junction is also ruled out as a source of the photocurrent. In a Schottky diode, in addition to the non-linearity of the I-Vs, the reverse and the forward saturation currents depend strongly on the temperature. This was not the case here.

4.3 Frequency dependent Measurements

The room temperature frequency response of light sensors is of much importance. We measured the frequency response for our PTV device by performing on-off photocurrent measurements.

The resultant measurement is shown in Figure 4-6. The ratio of the transient photocurrent, I_{photo}, to the root-mean-square dark current, RMS I_{dark} was found to be 25. The room temperature photocurrent was 38 μA for an incident power of 140 mW. The photocurrent increased and decreased sharply, with the response time shorter than 1 s, which was not observed in a previously published study of a similar PTV device based on carbon nanotubes or graphite [27, 28].

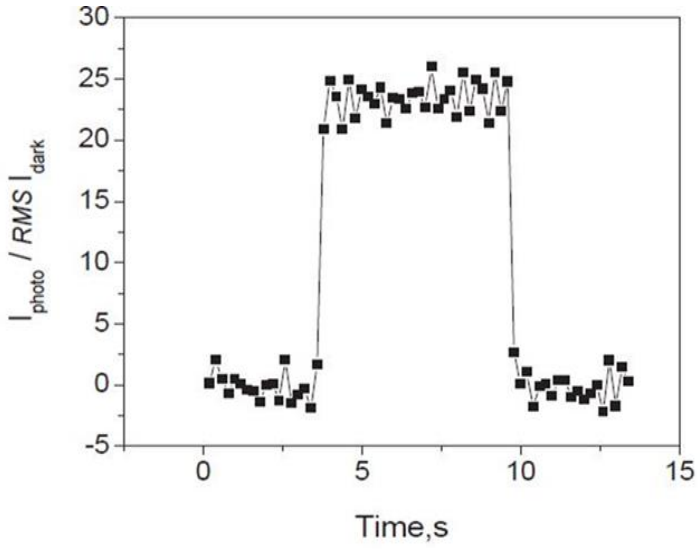

Figure 4-6. Ratio of the transient (on-off) photocurrent, I_{photo}, to the root-mean-square dark current, RMS I_{dark}.

We assessed the high-frequency response by modulating the incident intensity of a CW-1064 nm solid-state laser using an optical chopper and a Stanford Research System SR810 lock-in amplifier. The experiment setup is illustrated in Figure 4-7.

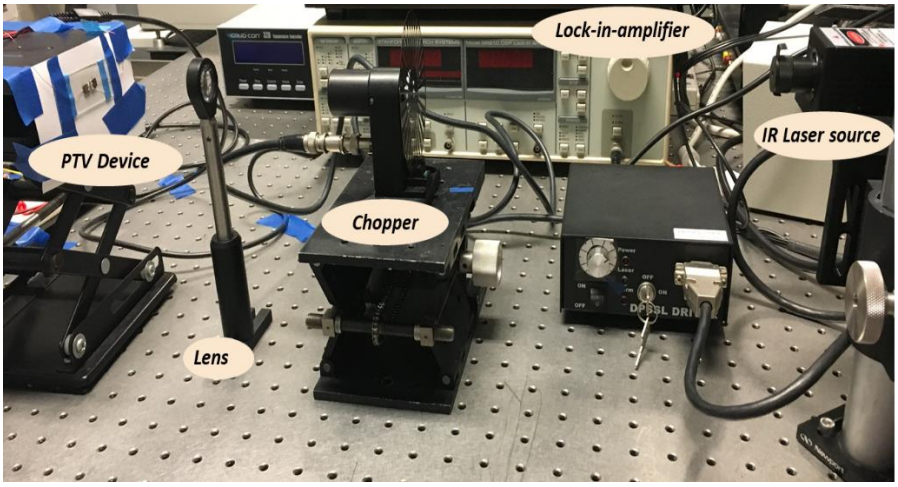

Figure 4-7. Experiment setup for the high-frequency response measurements.

Without applying any external bias, we measured the dependence of the alternating short-circuit current, I_{SC}, to the frequency, f, ranging from 50 Hz to 6 kHz for different excitation optical powers. Figure 4-8 reveals the results for the frequency range of 2 to 6 kHz. I_{SC} is approximately equivalent to $f^{-\alpha}$, where f is the frequency and $\alpha = 0.92 \pm 0.02$ independent of light intensity. The solid lines in Figure 4-8, indicate best-fit data for a log-log scale as obtained using Origin Lab 7.5.

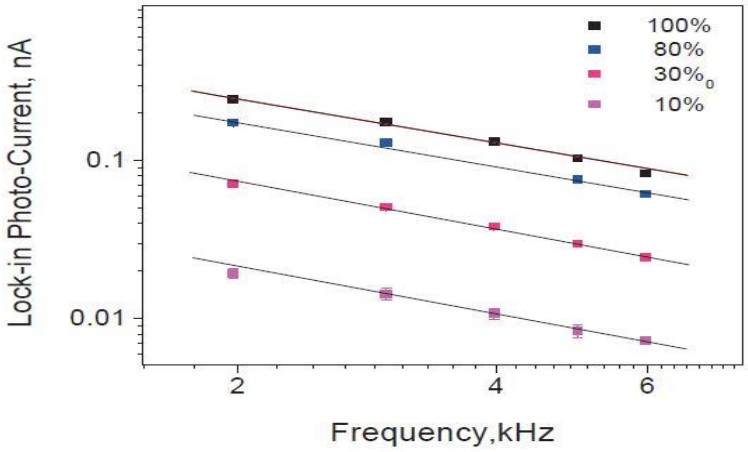

Figure 4-8. Dependency of the lock-in photocurrent on the frequency for different excitation powers.

We also investigated the photocurrent while varying the optical power by using neutral-density filters and modulating incident light at a high frequency (laser light was chopped at 4957 Hz). Figure 4-9 shows that the photocurrent changes linearly with respect to the optical power. As the sensor response time does not depend on the optical power, carrier-carrier scattering such as Auger recombination is insignificant.

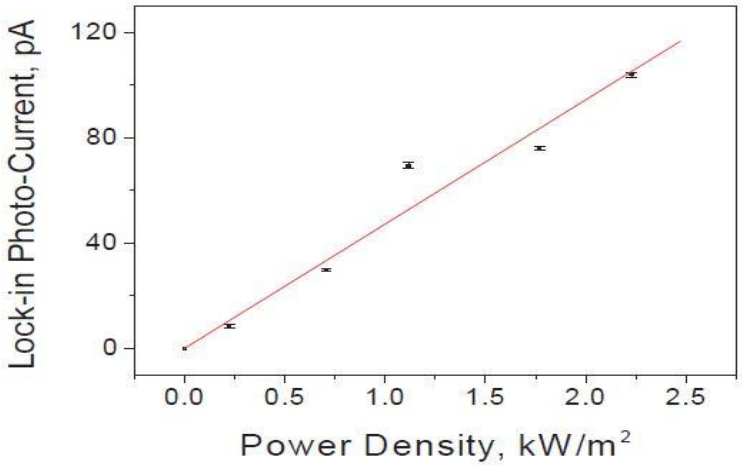

Figure 4-9. Lock-in photocurrent vs power density at the modulation frequency of 4975 Hz. The red line is the linear fit of the data.

Though the photocurrent of the device decreases at high frequencies, we conclude in the next section that a much smaller PTV device based on Cd_3As_2 is intrinsically fast and approaches the terahertz bandwidth.

4.4 Discussion of the bandwidth of a PTV device based on Cd_3As_2

The bandwidth of the detector based on Cd_3As_2 is specified by the thermal response time of the material which determines the response time of ΔV_{emf}, and is not limited by the device circuit impedance, Z. Assuming negligible contribution of the contact capacitance, the circuit impedance is

$$Z \cong R \,||\, C = \frac{R}{1 + jRC\omega}$$

in which $RC=\varepsilon/\sigma$. Given that the dielectric constant, $\varepsilon = 36\ \varepsilon_0$, and the electrical conductivity of Cd_3As_2, $\sigma = 2\times10^5$ S/m, the circuit response time of the detector, τ_{RC}, is on the order of 10^{-15}s. Therefore, for the frequencies below 10^{15} Hz (including the frequencies measured in this study), $Z \approx R$.

The upper bound frequency response of the device is found to be $f_{resp} \cong 0.35/\tau_r$ where τ_r is the rise time of the detector dependent on both RC-time constant τ_{RC} and the time required to form the temperature difference across the channel of the device τ_{tr} (rise time: $\tau_r = \sqrt{\tau_{RC}^2 + \tau_{tr}^2}$).

The speed and size of a fast sensor with the smallest τ_r can be estimated based on a transition reflectance study by Weber .et.al on Cd_3As_2 [29]. In that study, the photo-excited electrons and holes are allowed to relax by first emitting optical phonons on the time scale of 0.5 ps followed by emission of phonons within τ_{el}= 3.1 ps. According to them, the upper bound of the diffusion coefficient of the electrons (D), optically excited by photons with energy of 1.5 eV, is 60 cm^2/s. Therefore, given the diffusion length of the photoexcited electrons, $d^2 = D\ \tau_{el}$, the device channel length (L) is calculated to be on the order of d, for a fast rise time. Otherwise, the temperature gradient takes longer to form for a channel longer than the diffusion length.

Considering L=d, $\tau_r = \tau_{el} = L^2/D$, with τ_{el}= 3.1 ps and $D \leq 60\ cm^2/s$, the length of the channel, L, for a PTV device based on Cd_3As_2 is predicted to be $L \leq 60$ nm that can operate at a frequency up to 0.1 THz ($f_{resp} \cong 0.35/\tau_r$; τ_{el}= 3.1 picosecond).

Chapter 5.

Summary and Future Work

In this thesis, we described our synthesis of single crystals of Cd_3As_2 platelet using a chemical vapor deposition technique. The formation of the platelets was confirmed by scanning electron microscopy (SEM) images and energy dispersive X-ray spectroscopy (EDS). Fourier transform infrared spectroscopy (FTIR) at room temperature demonstrated strong absorption throughout the mid-infrared, implying that the sensor based on the Cd_3As_2 platelet can remain highly sensitive at long wavelength.

Temperature dependent transport and Seebeck measurements were performed on the Cd_3As_2 platelets. The temperature dependent current voltage measurements confirmed an Ohmic-like transport behavior. Temperature dependent Seebeck measurements showed a high thermopower at room temperature. Based on this, we engineered an infrared photodetector based on Cd_3As_2 platelet which made use of the optically induced Seebeck effect. The photocurrent of this photodetector depends on the optical power and modulation frequency and its responsivity reaches 0.27 mA/W – close to a similar two-terminal graphene sensor with a responsivity of 0.5 mA/W [30]. Thus, ours is a robust broad bandwidth photodetector which does not require an external bias.

Cd_3As_2 is a great candidate as a photo-thermo-sensing material due to its ultra-fast and spectrally broad response. Such a photo-thermo-voltaic device based on Cd_3As_2 can be further improved in responsivity and wavelength selectivity by patterning the detector surface using plasmonic nanostructures. Such structures are known to induce spatially non-uniform light heating, pushing the spatial resolution far below the wavelength of the light and the response frequency into the terahertz range [31,32].

References

1.W. Herschel, Experiments on the refrangibility of the invisible rays of the sun, Phi, Trans Royal, Soc, Lond, 90,284-292 (1800).

2.Infrared- Infrared radiation, Available at :https://www.infratec-infrared.com/sensor-division/service-support/glossary/infrared-radiation/. (Accessed: 16th December 2021)

3.E. S. Barr, The infrared pioneers-II. Macedonio Melloni, Infrared Phys, 2, 67-73 (1962).

4. G. Spingarn, S. S. Piatek, Infrared photodetectors: theory, practice, and applications, Available at: https://www.photonics.com/Webinar.aspx?WID=263. (Accessed 16th December 2021).

5. Infrared waves, Available at: https://science.nasa.gov/ems/07_infraredwaves, (Accessed 16th December 2021).

6. X. Lu, L. sun, P. Jiang, and X. Bao, Progress of photodetectors based on the photothermoelectric effect, Adv. Mater, 31, 1902044 (2019).

7. A. Rogalski, Infrared detectors: status and trends, ,Elsevier, Prog. Quantum Electron, 27,59 (2003).

8. A. Rogalski, HgCdTe photodetector material: history, status and outlook, Rep. Prog. Phys, 68, 2267 (2005).

9. P. Martyniuk and A. Rogalski, Hot infrared photodetectors ,Opto-Elector Rev, 2, 21, 240-258 (2013).

10.R. J. D. Tilley, Understanding solids, Wiley, 2nd ed, 15, 506 (2013).

11. T. Hosseini, Synthesis, transport, and thermoelectric studies of topological Dirac semimetal Cd_3As_2 for room temperature waste heat recovery and energy conversion, dissertation, UWM, Ch1, 6 (2017).

12.G. B. Halasz and L. Balents, Time -reversal invariant realization of the Weyl semimetal phase, Phys. Rev, B 85, 035103 (2012).

13.Y. Sakamoto, T. Hirahara, H. Miyazaki, S. Kimura, and S. Hasegawa, Spectroscopic evidence of a topological quantum phase transition in ultrathin Bi_2Se_3 films, Phys. Rev, B81, 165432 (2010).

14.J.Wang, A.M. DaSilva, C. Chang, K. He, J. K. Jain, N. Samarth, X. Ma, Q. Xue, and M. H. W. Chan, Evidence of electron-electron interaction in topological insulator thin films, Phys. Rev, B83, 245438 (2011).

15.T. Liang, Q. Gibson, M. N. Ali, M. Liu, R. J. Cava, and N. P. Ong ,Ultra-high mobility, and giant magnetoresistance in the Dirac semimetal Cd_3As_2, Nat. Mater, 14, 280 (2015).

16.T. Hosseini, N. Yavarishad, J. Alward, and N. Kouklin, Large thermopower, crystalline Cd_3As_2 by low-temperature vapor deposition for room temperature heat waste recovery, Advanced Electronic Materials, 2, 1500319 (2016).

17. J. R. Creighton, and P. Ho , Introduction to chemical vapor deposition (CVD), Sandia National lab, 1-22 (2001).

18. A. K. Pattanaik, and V. K. Sarin, Basic principles of CVD thermodynamics and kinetics, Sandia National lab, 23-43 (2001).

19.Optical thin films on complex substrate geometries, Available at : http://www.techbriefs.com/component/content/article/ntb/features/feature-articles/15991 (Accessed: 16th December 2021).

20.Scanning electron microscopy, Available at: https://fakultaeten.hu-berlin.de/en/mnf/forschung_internationales/grs/salsa/p-alabs/application-lab /instrumentation/a-labs-sem (Accessed: 16th December 2021).

21. Y. Leng, Materials Characterization, Introduction to Microscopic and Spectroscopic Methods, 121-144, Wiley (2008).

22. Y. Leng, Materials Characterization, Introduction to Microscopic and Spectroscopic Methods, 171-196, Wiley (2008).

23. Y. Leng, Materials Characterization, Introduction to Microscopic and Spectroscopic Methods, 253-300, Wiley (2008).

24. As-Cd phase diagram, Available at : http://www.himikatus.ru/art/phase-diagr1/As-Cd.php (Accessed: 16th December 2021).

25. N. Kouklin, M. Tzolov, D. Straus, and J. M. Xu, Infrared absorption properties of carbon nanotubes synthesized by chemical vapor deposition, Apply. Phys. Lett.85, 4463 (2004).

26. N. Yavarishad, T. Hosseini, E. Kheirandish, C. P. Weber, and N. Kouklin, Room-temperature Self-powered Energy Photodetector Based on Optically Induced Seebeck effect in Cd_3As_2, Appl Phys Exp,10 (5),052201 (2017).

27. M. Omari, N. Kouklin, Photothermovoltaic effect in carbon nanotubes: En route toward junctionless infrared photocells and light sensors, Appl. Phys. Lett., 98, 243113, (2011).

28. T. Hosseini and N. Kouklin, On plasmon-induced photocurrent and doping of metal-patterned graphene, Appl. Phys. Lett. 98,243113 (2011).

29. C. P. Weber, E. Arushanov, B. S. Berggren, T. Hosseini, N. Kouklin, A. Nateprov, Transient reflectance of photoexcited Cd_3As_2, Appl. Phys. Lett., 106, 231904 (2015).

30. F. Xia, T. Muller, Y. Lin, A. Valdes-Garcia, and P. Avouris, Ultrafast graphene photodetector, Nat. Nanothechnol, 4, 839 (2009).

31. T. Hosseini, N. Kouklin, On plasmon-induced photocurrent and doping of metal-patterned graphene, Appl. Phys. Lett, 105, 043104 (2014).

32. J. A. Schuller, E. S. Barnard, W. Cai, Y.C. Jun, J.S. White, and M. L. Brongersma, Plasmonic for extreme light concentration and manipulation , Nat. Matt. 9, 193 (2010).